Transient Dynamic Crack Analysis by a Hypersingular Time-Domain BEM

Ch. Zhang

Department of Civil Engineering, Hochschule Zittau/Görlitz, University of Applied Sciences,
D-02763 Zittau, Germany

ABSTRACT

This paper presents a two-dimensional (2-D) hypersingular time-domain traction BEM for transient dynamic crack analysis of isotropic and linearly elastic solids. Hypersingular time-domain traction boundary integral equations (BIEs) are applied. A time-stepping scheme based on collocation method for spatial discretization is developed for solving the time-domain BIEs numerically. A linear temporal shape-function is adopted, while two different shape-functions are used for simplicity. For elements adjacent to crack-tips, a square-root crack-tip shape-function is applied, while a constant shape-function is used for elements away from crack-tips. The arising hypersingular and strongly singular integrals are computed analytically and numerically. Numerical results for dynamic stress intensity factors are presented to show the efficiency and the accuracy of the present hypersingular time-domain BEM.

INTRODUCTION

Time-domain boundary element method (BEM) is very promising for solving transient dynamic crack problems in linearly elastic solids. Since the classical displacement BEM is not suitable for crack analysis without domain-substructuring, several alternative BEM formulations have been proposed in past years, for instance, the Green's function BEM, the Dual BEM, and the traction BEM ([1]-[8]). In this paper, a hypersingular time-domain traction BEM for transient dynamic crack analysis is presented. The method applies hypersingular time-domain traction boundary integral equations (BIEs), both to crack-faces and external boundaries of a cracked solid. The essential advantage of the method is that no domain-substructuring is required, and only one type of BIEs is needed. Hypersingular traction BIEs are obtained by substituting the representation formula for displacements into Hooke's law and taking the usual limiting process. The arising hypersingular integrals are regarded as Hadamard finite-part integrals. To solve the hypersingular time-domain traction BIEs numerically, various methods such as the Galerkin method, the regularization method, and the direct method can be applied. A direct method is adopted in this analysis. Hypersingular time-domain BEM for transient dynamic crack analysis has been presented previously in [9]-[13].

A time-stepping scheme is developed for solving hypersingular time-domain traction BIEs for 2-D elastodynamic crack problems. The scheme uses a linear temporal shape-function for temporal discretization and a collocation method for spatial discretization. Time integrations arising in computing the system matrices are carried out analytically. For simplicity, two different spatial shape-functions are adopted for spatial discretization: a square-root crack-tip shape-function for elements adjacent to crack-tips, and a constant shape-function for elements away from crack-tips. The square-root crack-tip shape-function describes the local behavior of the crack-opening-displacements (CODs) at crack-tips properly, and its use ensures an accurate numerical computation of the dynamic stress intensity factors from the CODs directly. The spatial approximation of the boundary displacements and boundary tractions is done by using a constant spatial shape-function. To evaluate hypersingular and strongly singular spatial integrals in computing the system matrices, a semi-analytical singularity-subtraction technique is applied ([13], [14]). The present hypersingular time-domain BEM is suitable for both infinite and finite solids with straight or curved cracks subjected to any kind of time-dependent dynamic loadings. To show the accuracy and the efficiency of the present time-domain BEM, numerical examples for infinite and finite linearly elastic solids with cracks are given.

HYPERSINGULAR TIME-DOMAIN TRACTION BIES

Let us consider a finite crack contained in a two-dimensional (2-D), homogeneous, isotropic and linearly elastic solid as shown in Fig. 1. Without body forces, the cracked solid shall satisfy the equations of motion [15]

$$\sigma_{\alpha\beta,\beta} = \rho \ddot{u}_\alpha, \tag{1}$$

the Hooke's law

$$\sigma_{\alpha\beta} = E_{\alpha\beta\gamma\delta} u_{\gamma,\delta}, \tag{2}$$

the initial conditions

$$u_\alpha(\mathbf{x},t) = \dot{u}_\alpha(\mathbf{x},t) = 0\,, \qquad t \leq 0, \tag{3}$$

and the boundary conditions

$$\begin{aligned} f_\alpha(\mathbf{x},t) &= 0\,, & \mathbf{x} \in \Gamma_c, \qquad (4)\\ f_\alpha(\mathbf{x},t) &= f_\alpha^*(\mathbf{x},t)\,, & \mathbf{x} \in \Gamma_\sigma, \qquad (5)\\ u_\alpha(\mathbf{x},t) &= u_\alpha^*(\mathbf{x},t)\,, & \mathbf{x} \in \Gamma_u\,, \qquad (6) \end{aligned}$$

where $f_\alpha(\mathbf{x},t) = \sigma_{\alpha\beta}(\mathbf{x},t)n_\beta$ denotes the traction components, $\sigma_{\alpha\beta}$ and u_α the stress and the displacement components, ρ the mass density, $E_{\alpha\beta\gamma\delta}$ the elasticity tensor, n_β the unit normal vector, $\Gamma_c = \Gamma_c^+ + \Gamma_c^-$ with $\Gamma_c^\pm$ being the upper and the lower crack-faces, Γ_σ the extrenal boundary where the stresses or the tractions f_α^* are given, and Γ_u represents the external boundary where the displacements u_α^* are prescribed, respectively. Throughout the analysis, a comma after a quantity stands for spatial derivatives, while superscript dots designate temporal derivatives of the quantity. The conventional summation rule over double indices is applied, with Greek indices $\alpha, \beta, \gamma = 1, 2$.

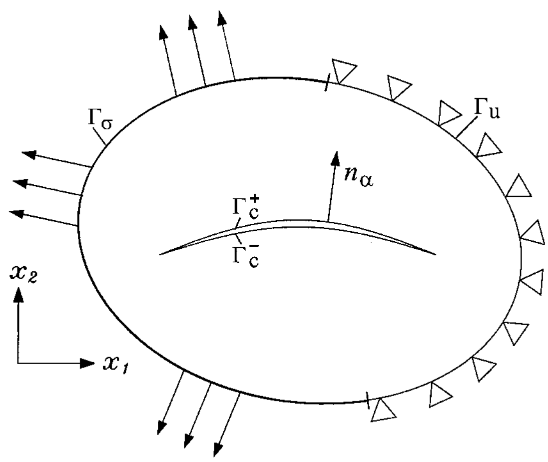

Fig. 1: A finite crack in a finite solid

The displacement field $u_\gamma(\mathbf{x},t)$ can be represented by a boundary integral

$$u_\gamma(\mathbf{x},t) = \int\limits_{\Gamma_\sigma+\Gamma_u} \left(u_{\alpha\gamma}^G * \sigma_{\alpha\beta} - \sigma_{\alpha\beta\gamma}^G * u_\alpha\right) n_\beta ds + \int\limits_{\Gamma_c^+} \sigma_{\alpha\beta\gamma}^G * \Delta u_\alpha n_\beta ds, \quad \mathbf{x} \in \Omega, \tag{7}$$

with $\Delta u_\alpha(\mathbf{y},\tau)$ being the crack-opening-displacements (CODs) defined by

$$\Delta u_\alpha(\mathbf{y},t) = u_\alpha(\mathbf{y} \in \Gamma_c^+, \tau) - u_\alpha(\mathbf{y} \in \Gamma_c^-, \tau). \tag{8}$$

The usual limiting process $\mathbf{x} \to \Gamma_c^\pm$ applied to Eq. (7) leads to a degenerate BIE formulation for crack analysis. To overcome this difficulty, a hypersingular time-domain traction BIE formulation is used in this paper. By substituting Eq. (7) into Hooke's law (2), taking the limit $\mathbf{x} \to \Gamma_\sigma + \Gamma_u + \Gamma_c^+$ and considering the boundary conditions (4)-(6), time-domain traction BIEs are obtained as

$$\delta(\mathbf{x}) f_\alpha(\mathbf{x},t) = n_\beta(\mathbf{x}) \int\limits_{\Gamma_\sigma+\Gamma_u} \left(U_{\gamma\alpha\beta}^G * f_\gamma - T_{\gamma\alpha\beta}^G * u_\gamma\right) ds + n_\beta(\mathbf{x}) \int\limits_{\Gamma_c^+} T_{\gamma\alpha\beta}^G * \Delta u_\gamma ds, \qquad \mathbf{x} \in \Gamma, \tag{9}$$

in which

$$\delta(\mathbf{x}) = \begin{cases} \dfrac{1}{2}, & \mathbf{x} \in \Gamma_\sigma + \Gamma_u\,, \\ 1, & \mathbf{x} \in \Gamma_c\,, \end{cases} \tag{10}$$

and

$$U_{\gamma\alpha\beta}^G = -E_{\alpha\beta\delta\lambda} u_{\delta\gamma,\lambda}^G = -\sigma_{\alpha\beta\gamma}^G\,, \qquad T_{\gamma\alpha\beta}^G = -E_{\alpha\beta\delta\lambda} \sigma_{\gamma\eta\delta,\lambda}^G n_\eta\,, \tag{11}$$

where sufficiently smooth boundaries Γ_σ and Γ_σ are assumed, and $U^G_{\gamma\alpha\beta}$ and $T^G_{\gamma\alpha\beta}$ are 2-D time-domain Green's functions. Note here that the time-domain traction BIEs (9) are hypersingular because

$$T^G_{\gamma\alpha\beta}(\mathbf{x}, t; \mathbf{y}, \tau) \propto \frac{1}{\mid \mathbf{x} - \mathbf{y} \mid^2}, \qquad \text{as} \quad \mathbf{x} \to \mathbf{y}. \tag{12}$$

The hypersingular integrals are regarded as Hadamard finite-part integrals, which can be evaluated analytically and numerically [14].

TIME-STEPPING SCHEME

To solve the hypersingular time-domain traction BIEs (9) numerically, the crack-face, the external boundaries and the time variable t are discretized as

$$\Gamma = \sum_{e=1}^{E} \Gamma_e, \qquad t = \sum_{n=1}^{N} n\Delta t, \tag{13}$$

where $\Gamma = \Gamma_\sigma + \Gamma_u + \Gamma_c^+$ with Γ_e representing the e-th element, $E = E_1 + E_2$ is the total element-number with E_1 and E_2 being the element-numbers for the crack and the external boundaries, and Δt is a constant time-step. The unknown CODs and other boundary data are approximated by using the following interpolation functions

$$\Delta u_\gamma(\mathbf{y}, \tau) = \sum_{e=1}^{E_1} \sum_{n=1}^{N} \mu_{e(\Delta u)}(\mathbf{y}) \eta^n_{(\Delta u)}(\tau) (\Delta u_\gamma)^n_e, \tag{14}$$

$$u_\gamma(\mathbf{y}, \tau) = \sum_{e=1}^{E_2} \sum_{n=1}^{N} \mu_{e(u)}(\mathbf{y}) \eta^n_{(u)}(\tau) (u_\gamma)^n_e, \tag{15}$$

$$f_\gamma(\mathbf{y}, \tau) = \sum_{e=1}^{E_2} \sum_{n=1}^{N} \mu_{e(f)}(\mathbf{y}) \eta^n_{(f)}(\tau) (f_\gamma)^n_e, \tag{16}$$

in which $\mu_{e(\cdot)}(\mathbf{y})$ and $\eta^n_{(\cdot)}(\tau)$ denote the spatial and the temporal shape-functions. The spatial shape-function is chosen as

$$\mu_{e(\cdot)}(\mathbf{y}) = g_{(\cdot)}(\mathbf{y}) H(\mathbf{y}) = \begin{cases} g_{(\cdot)}(\mathbf{y}), & \mathbf{y} \in \Gamma_e, \\ 0, & \mathbf{y} \notin \Gamma_e, \end{cases} \tag{17}$$

with the function $g_{(\cdot)}(\mathbf{y})$ describing the spatial variation of the unknown data in the e-th element and $H(\mathbf{y})$ being the Heaviside function. The temporal variation of the unknown boundary data is approximated by a linear temporal shape-function of the form

$$\eta^n_{(\Delta u)}(\tau) = \eta^n_{(u)}(\tau) = \eta^n_{(f)}(\tau) = \begin{cases} 1 - \dfrac{\mid \tau - n\Delta t \mid}{\Delta t}, & \mid \tau - n\Delta t \mid \leq \Delta t, \\ 0, & \text{otherwise}. \end{cases} \tag{18}$$

By using Eqs. (14)-(16), the hypersingular time-domain BIEs (9) can be converted into a system of linear algebraic equations as

$$\sum_{n=1}^{N} \left[\sum_{e=1}^{E_1} A^{mn}_{\gamma\alpha;ed} (\Delta u_\gamma)^n_e + \sum_{e=1}^{E_2} B^{mn}_{\gamma\alpha;ed} (u_\gamma)^n_e + \sum_{e=1}^{E_2} C^{mn}_{\gamma\alpha;ed} (f_\gamma)^n_e \right] = \delta_d (f_\alpha)^m_d, \tag{19}$$

where $\delta_d = \delta(\mathbf{x}_d)$ and the system matrices $A^{mn}_{\gamma\alpha;ed}$, $B^{mn}_{\gamma\alpha;ed}$ and $C^{mn}_{\gamma\alpha;ed}$ are given by

$$A^{mn}_{\gamma\alpha;ed} = n_\beta(\mathbf{x}_d) \int_{t_{n-1}}^{t_{n+1}} \left[\int_{\Gamma_e} T^G_{\gamma\alpha\beta}(\mathbf{x}_d, t_m; \mathbf{y}, \tau) \mu_{e(\Delta u)}(\mathbf{y}) ds \right] \eta^n_{(\Delta u)}(\tau) d\tau, \tag{20}$$

$$B^{mn}_{\gamma\alpha;ed} = -n_\beta(\mathbf{x}_d) \int_{t_{n-1}}^{t_{n+1}} \left[\int_{\Gamma_e} T^G_{\gamma\alpha\beta}(\mathbf{x}_d, t_m; \mathbf{y}, \tau) \mu_{e(u)}(\mathbf{y}) ds \right] \eta^n_{(u)}(\tau) d\tau, \tag{21}$$

$$C^{mn}_{\gamma\alpha;ed} = n_\beta(\mathbf{x}_d) \int\limits_{t_{n-1}}^{t_n+1} \left[\int\limits_{\Gamma_e} U^G_{\gamma\alpha\beta}(\mathbf{x}_d, t_m; \mathbf{y}, \tau)\mu_{e(f)}(\mathbf{y})ds \right] \eta^n_{(f)}(\tau)d\tau. \tag{22}$$

The use of a linear temporal shape-function (18) enables us to perform the arising time-integrations in computing the system matrices $A^{mn}_{\gamma\alpha;ed}$, $B^{mn}_{\gamma\alpha;ed}$ and $C^{mn}_{\gamma\alpha;ed}$ analytically. After analytical time-integrations the system matrices take the following forms

$$A^{mn}_{\gamma\alpha;ed} = n_\beta(\mathbf{x}_d) \int\limits_{\Gamma_e} T^*_{\gamma\alpha\beta}(\mathbf{x}_d, t_m; \mathbf{y}, t_n)\mu_{e(\Delta u)}(\mathbf{y})ds \tag{23}$$

$$B^{mn}_{\gamma\alpha;ed} = -n_\beta(\mathbf{x}_d) \int\limits_{\Gamma_e} T^*_{\gamma\alpha\beta}(\mathbf{x}_d, t_m; \mathbf{y}, t_n)\mu_{e(u)}(\mathbf{y})ds\,, \tag{24}$$

$$C^{mn}_{\gamma\alpha;ed} = n_\beta(\mathbf{x}_d) \int\limits_{\Gamma_e} U^*_{\gamma\alpha\beta}(\mathbf{x}_d, t_m; \mathbf{y}, t_n)\mu_{e(f)}(\mathbf{y})ds\,, \tag{25}$$

in which $T^*_{\gamma\alpha\beta}$ and $U^*_{\gamma\alpha\beta}$ are given by

$$\begin{aligned} T^*_{\gamma\alpha\beta} &= \int\limits_{(n-1)\Delta t}^{(n+1)\Delta t} T^G_{\gamma\alpha\beta}(\mathbf{x}_d, t_m; \mathbf{y}, \tau)\eta^n_{(u)}(\tau)d\tau \\ &= \frac{\mu}{(2\pi c_T \Delta t) r^2} \left[-\frac{2}{\kappa^3}(D^L_{\gamma\alpha\beta} + E^L_{\gamma\alpha\beta})P_L + 2(D^T_{\gamma\alpha\beta} + E^T_{\gamma\alpha\beta})P_T \right. \\ &+ \left. \left(\frac{4}{3r^2}\right) C_{\gamma\alpha\beta} \left(\frac{1}{\kappa^3}Q_L - Q_T\right) - r^2 \left(\frac{1}{\kappa^3} D^L_{\gamma\alpha\beta} S_L - D^T_{\gamma\alpha\beta} S_T\right) \right], \end{aligned} \tag{26}$$

$$\begin{aligned} U^*_{\gamma\alpha\beta} &= \int\limits_{(n-1)\Delta t}^{(n+1)\Delta t} U^G_{\gamma\alpha\beta}(\mathbf{x}_d, t_m; \mathbf{y}, \tau)\eta^n_{(f)}(\tau)d\tau \\ &= \frac{1}{(2\pi c_T \Delta t) r} \left[\frac{1}{\kappa^3} B^L_{\alpha\beta\gamma} P_L - B^T_{\alpha\beta\gamma} P_T - \left(\frac{1}{3r^2}\right) A_{\alpha\beta\gamma} \left(\frac{1}{\kappa^3}Q_L - Q_T\right) \right], \end{aligned} \tag{27}$$

where $r = |\mathbf{x}_d - \mathbf{y}|$, $\kappa = c_L/c_T$, c_L and c_T are the longitudinal and the transverse wave velocities defined by

$$c_L = \sqrt{\frac{\lambda + 2\mu}{\rho}}, \qquad c_T = \sqrt{\frac{\mu}{\rho}}, \tag{28}$$

with λ and μ being Lamé's elastic constants, and the auxilliary functions are given by

$$P_\xi = \sum_{q=-1}^{+1} (-2)^{1-|q|} H[(m-n+q)c_\xi \Delta t - r] \sqrt{(m-n+q)^2 (c_\xi \Delta t)^2 - r^2}\,, \tag{29}$$

$$Q_\xi = \sum_{q=-1}^{+1} (-2)^{1-|q|} H[(m-n+q)c_\xi \Delta t - r] \sqrt{[(m-n+q)^2 (c_\xi \Delta t)^2 - r^2]^3}\,, \tag{30}$$

$$S_\xi = \sum_{q=-1}^{+1} (-2)^{1-|q|} \frac{H[(m-n+q)c_\xi \Delta t - r]}{\sqrt{(m-n+q)^2 (c_\xi \Delta t)^2 - r^2}}\,, \tag{31}$$

in which $\xi = L, T$. Explicit expressions of the auxiliary functions $A_{\alpha\beta\gamma}$, $B^\xi_{\alpha\beta\gamma}$, $C_{\gamma\alpha\beta}$, $D^\xi_{\gamma\alpha\beta}$ and $E^\xi_{\gamma\alpha\beta}$ can be found in [13].

For $\mathbf{x}_d \notin \Gamma_e$, all integrals in the the system matrices (23)-(25) are regular and they can be computed numerically by using standard Gaussian quadrature. For $\mathbf{x}_d \in \Gamma_e$, Eqs. (23)-(24) may have hypersingularities, while strong singularities may arise in Eq. (25). In this case, the hypersingular and the strongly singular integrals can be computed analytically and numerically, see [13] for details.

To simplify the analysis, two different spatial shape-functions are applied to approximate the spatial variation of the unknown CODs. For elements adjacent to crack-tips, a square-root crack-tip shape-function is adopted, while for elements away from crack-tips a constant spatial shape-function is used. The square-root crack-tip shape-function describes the local behavior of the unknown CODs at crack-tips properly and thus ensures an accurate numerical computation from the CODs directly. Furthermore, the square-root crack-tip shape-function is also used for the second element ("transition element") behind the crack-tips. The "transition element" improves the accuracy of the numerical procedure for computing dynamic stress intensity factors. For simplicity, both the boundary displacements and the boundary tractions are approximated by a constant spatial shape-function. It should be noted here that an integrable singularity exists at the wave fronts $c_L(t-\tau) = r$ and $c_T(t-\tau) = r$, but it can be treated numerically by using standard Gaussian quadrature without difficulties.

In matrix and vector notations, the system of linear algebraic equations (19) can be rewritten as

$$\bar{\mathbf{A}}^1\mathbf{v}^q = \bar{\mathbf{C}}^1\mathbf{f}^q + \sum_{s=1}^{q-1}\left(\bar{\mathbf{C}}^{q-s+1}\mathbf{f}^s - \bar{\mathbf{A}}^{q-s+1}\mathbf{v}^s\right), \tag{32}$$

with the matrix $\bar{\mathbf{A}}^s$ consisting of the matrices $\mathbf{A}^s$ and $\mathbf{B}^s$, the matrix $\bar{\mathbf{C}}^s$ consisting of the matrix $\mathbf{C}^s$ and the unit matrix $\mathbf{I}$, $\mathbf{v}^s$ being a vector containing the CODs on the crack-face and the boundary displacements on external boundaries, and $\mathbf{f}^s$ being a vector of boundary tractions. By considering the boundary conditions (4)-(6), Eq. (32) can be recast into the following form

$$\bar{\mathbf{B}}^1\mathbf{x}^q = \bar{\mathbf{D}}^1\mathbf{y}^q + \sum_{s=1}^{q-1}\left(\bar{\mathbf{C}}^{q-s+1}\mathbf{f}^s - \bar{\mathbf{A}}^{q-s+1}\mathbf{v}^s\right), \tag{33}$$

where $\bar{\mathbf{B}}^1$ and $\bar{\mathbf{D}}^1$ are rearranged matrices from $\bar{\mathbf{A}}^1$ and $\bar{\mathbf{C}}^1$ according to the boundary conditions, $\mathbf{x}^q$ is a vector containig the unknown boundary data, and $\mathbf{y}^q$ is a vector containig the known or given boundary data f_α^* and u_α^*. Finally, Eq. (33) yields the following time-stepping scheme

$$\mathbf{x}^q = (\bar{\mathbf{B}}^1)^{-1}\left[\bar{\mathbf{D}}^1\mathbf{y}^q + \sum_{s=1}^{q-1}\left(\bar{\mathbf{C}}^{q-s+1}\mathbf{f}^s - \bar{\mathbf{A}}^{q-s+1}\mathbf{v}^s\right)\right], \qquad (q = 1, 2, ..., N), \tag{34}$$

with $\bar{\mathbf{B}}^1$ being the system matrix at the first time-step and $(\bar{\mathbf{B}}^1)^{-1}$ being its inverse. By using Eq. (34), the unknown CODs, boundary displacements and boundary tractions can be computed numerically time-step by time-step.

NUMERICAL EXAMPLES

To show the efficiency and the accuracy of the present hypersingular time-domain traction BEM, numerical examples are presented in the following. For convenience, the dynamic stress intensity factors are normalized by

$$\bar{K}_i(t) = K_i(t)/K_i^{st}, \qquad (i = I,\, II), \tag{35}$$

where

$$K_I^{st} = \sigma_{22}\sqrt{\pi a}, \qquad K_{II}^{st} = \sigma_{12}\sqrt{\pi a} \tag{36}$$

are the corresponding static stress intensity factors for a finite crack of length $2a$ in an infinite solid subject to static stresses σ_{22} and σ_{12} on the crack-faces.

We first consider a finite crack of length $2a$ contained in an infinite and linearly elastic solid as shown in Fig. 2. Plane strain is assumed and Possion's ratio is taken as $\nu = 0.25$. The crack is discretized by 20 elements and a time-step of $\Delta t = 0.1a/c_T$ is applied. The selected time-step corresponds to a time needed by a transverse wave to travel one element-length.

For an impact tensile and shear loading applied on the crack-faces as depicted in Fig. 2, the normalized mode I and mode II dynamic stress intensity factors are shown in Fig. 3 versus the dimensionless time c_Tt/a. Here, the superscript "$\pm$" stands for the left and the right crack-tips. For comparison purpose, the corresponding analytical results of Thau and Lu [16] are also given in Fig. 3. Thau and Lu [16] applied a Wiener-Hopf technique for solving their singular integral equations and they could obtain analytical solutions in the small-time range. The comparison shows that the present time-domain BEM provides very good numerical results which agree very well with the analytical results of Thau and Lu [16]. Thau and Lu [16] have shown that the peaks arise at a time which is needed by a Rayleigh-wave to travel from one crack-tip to another. The dynamic stress intensity factors overshoot their corresponding static values by maximum 30%. An additional check for the present time-domain BEM has been made by comparing the numerically computed dynamic stress intensity factors in the long-time limit with the exact results $\bar{K}_I^{\pm}(t=\infty) = \bar{K}_{II}^{\pm}(t=\infty) = 1$. The comparison shows that the numerically computed dynamic stress intensity factors in the long-time limit deviate from the exact results $\bar{K}_I^{\pm}(t=\infty) = \bar{K}_{II}^{\pm}(t=\infty) = 1$ by less than 3%.

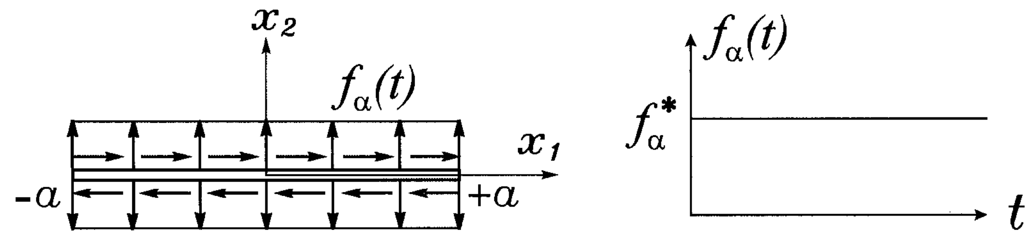

Fig. 2: A finite crack in an infinite solid under an impact loading

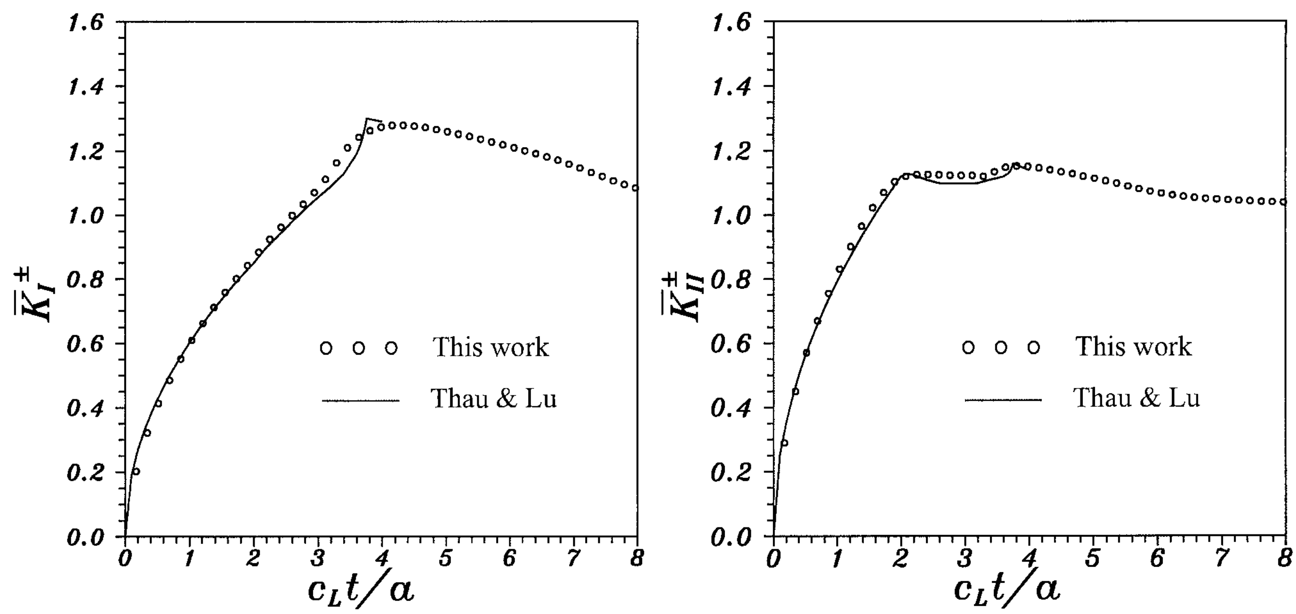

Fig. 3: Normalized mode I and mode II dynamic stress intensity factors

Next, a finite rectangular plate with an inclined edge crack of length a in plane strain is considered, see Fig. 4. The used material and geometrical data for numerical calculations are given in Fig. 4. An impact tensile loading is applied on the upper boundary of the cracked plate, while on other plate boundaries mixed boundary conditions are supplied as shown in Fig. 4. The plate boundaries and the crack are discretized by using 87 elements: 32 for the horizontal, 44 for the vertical plate boundaries, and 11 for the crack. A time-step $\Delta t = (B/32)/c_L = 0.15804\mu s$ is used, with B being the plate width.

Figure 5 shows the normalized dynamic stress intensity factors $\bar{K}_I(t)$ and $\bar{K}_{II}(t)$ versus time t. For the purpose of comparison, numerical results of Domínguez and Gallego [17], Fedelinski *et al.* [18], and Murti and Valliapan [19] are also presented in Fig. 5. Domínguez and Gallego [17] used a time-domain displacement BEM in conjunction with a multi-domain method, Fedelinski *et al.* [18] applied a Laplace transform dual BEM, and Murti and Valliapan [19] used a finite element method to obtain dynamic stress intensity factors numerically. It can be seen on Fig. 5 that in the small-time range the numerical results provided by the present time-domain traction BEM agree very well with those of other authors. In despite of some discrepancies, the agreement between the present numerical results and others in the large-time range is still satisfactory. Possible reasons for the discrepancies between the numerical results of different athors in the large-time range could be the differently applied time-steps and methods for computing the dynamic stress intensity factors.

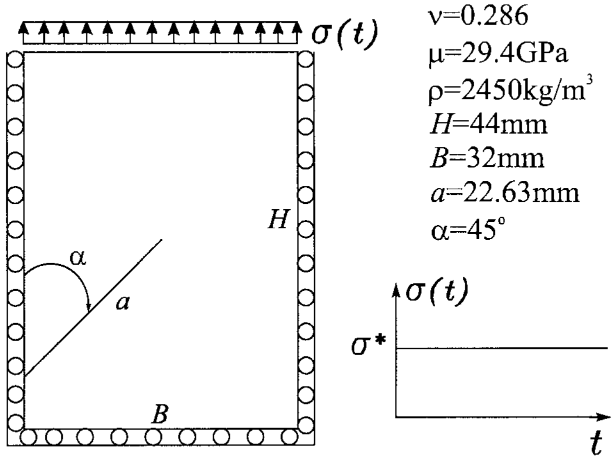

Fig. 4: A rectangular plate with an inclined edge crack

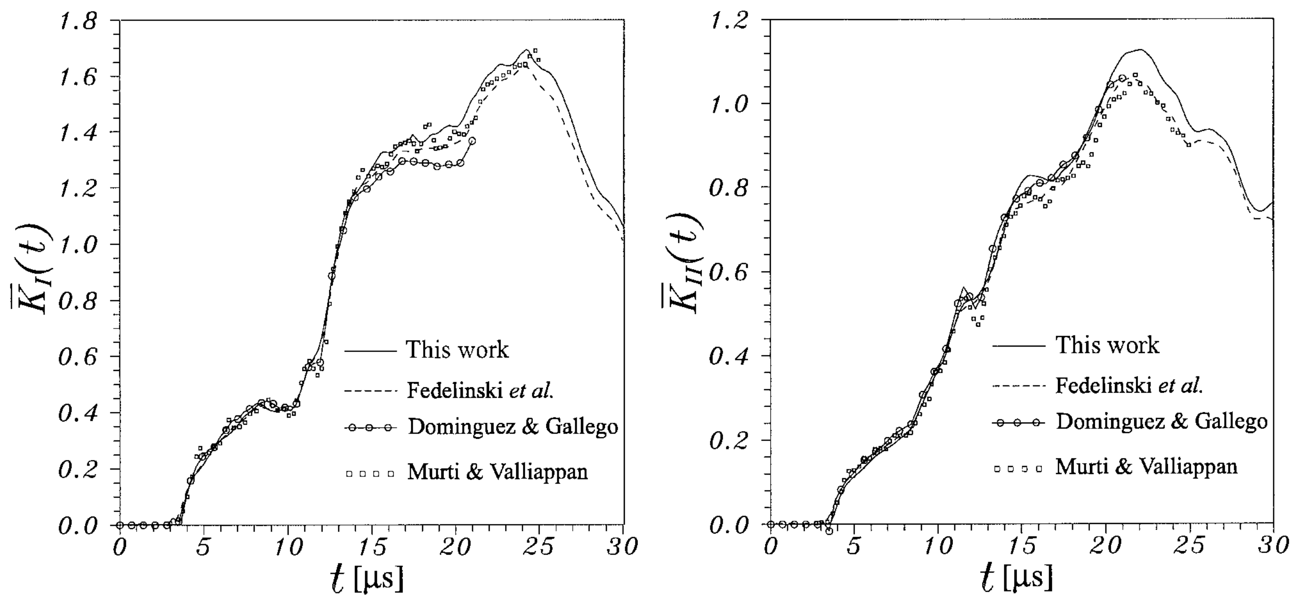

Fig. 5: Normalized mode I and mode II dynamic stress intensity factors

CONCLUSIONS

A hypersingular time-domain traction BEM for 2-D transient dynamic crack analysis is presented. Hypersingular time-domain traction BIEs are applied to both crack-faces and external boundaries. The method uses a linear temporal shape-function for the unknwon CODs, boundary displacements and boundary tractions. Two different spatial shape-functions for the CODs are adopted. A square-root crack-tip shape-function is used for elements adjacent to crack-tips, while a constant spatial shape-function is applied for elements away from crack-tips. Boundary displacements and boundary tractions are approximated by a constant spatial shape-function. The use of the square-root crack-tip shape-shape function ensures a proper description of the local behavior of CODs at crack-tips and an accurate numerical computation of the dynamic stress intensity factors from CODs directly. Numerical examples for cracked infinite and finite solids show that the present time-domain traction BEM is highly efficient and accurate for transient dynamic crack analysis.

RERERENCES

[1] Aliabadi, M.H. and Rooke, D.P., *Numerical Fracture Mechanics*, Computational Mechanics Publications, Southampton, UK & Boston, USA, 1991.

[2] Tanaka, M., Sládek, V. and Sládek J., "Regularization Techniques Applied to Boundary Element Methods", *Appl. Mech. Rev.*, Vol. 47, 1994, pp. 457-499.

[3] Aliabadi, M.H., "Boundary Element Formulations in Fracture Mechanics", *Appl. Mech. Rev.*, Vol. 50, 1997, pp. 83-96.

[4] Beskos, D.E., "Boundary Element Methods in Dynamic Analysis: Part II (1986-1996)", *Appl. Mech. Rev.*, Vol. 50, 1997, pp. 149-197.

[5] Zhang, Ch. and Gross, D., *On Wave Propagation in Elastic Solids With Cracks*, Computational Mechanics Publications, Southampton, UK & Boston, USA, 1997.

[6] Richardson, J.D. and Cruse, T.A., "Nonsingular BEM for Fracture Modelling", *Comp. Struct.*, Vol. 66, 1998, pp. 695-703.

[7] Bonnet, M., *Boundary Integral Equation Methods for Solids and Fluids*, John Wiley & Sons Ltd, 1999.

[8] Chen, J.T., "Review of Dual Boundary Element Methods with Emphasis on Hypersingular Integrals and Divergent Series", *Appl. Mech. Rev.*, Vol. 52, 1999, pp. 17-33.

[9] Gallego, R. and Domínguez, J., "Hypersingular BEM for Transient Elastodynamics", *Int. J. Numer. Meth. Engng.*, Vol. 39, 1996, pp. 1681-1705.

[10] Zhang, Ch. and Savaidis, A., "A Hypersingular BEM for Dynamic Crack Analysis", *ZAMM Z. Angew. Math. Mech.*, 1999, Vol. 79.

[11] Zhang, Ch. and Savaidis, A., "Time-Domain BEM for Dynamic Crack Analysis", *Mathematics and Computers in Simulation*, Vol. 50, 1999, pp. 351-362.

[12] Zhang, Ch. and Savaidis, A., "Dynamic Crack Analysis by Hypersingular and Non-Hypersingular Time-Domain BEM", *Proceedings of the IUTAM/IACM/IABEM Symposium on Mathematical and Computational Mechanics Aspects of the Boundary Element Method*, Kluwer Academic Publishers, in press, 2001.

[13] Zhang, Ch., "A 2-D Hypersingular Time-Domain Traction BEM for Transient Elastodynamic Crack Analysis", *Wave Motion*, in press, 2001.

[14] Sládek, V. and Sládek, J. (Eds.), *Singular Integrals in Boundary Element Methods*, Computational Mechanics Publications, Southampton, UK & Boston, USA, 1998.

[15] Achenbach, J.D., *Wave Propagation in Elastic Solids*, North-Holland, Amsterdam/New York, 1973.

[16] Thau, S.A. and Lu, T.H., "Transient Stress Intensity Factors for a Finite Crack in an Elastic Solid Caused by a Dilatational Wave", *Int. J. Solids Struct.*, Vol. 7, 1971, pp. 731-750.

[17] Domínguez, J. and Gallego, R., "Time Domain Boundary Element Method for Dynamic Stress Intensity Factor Computations", *Int. J. Numer. Meth. Engng.*, Vol. 33, 1992, pp. 635-647.

[18] Fedelinski, P., Aliabadi, M.H. and Rooke, D.P., "The Laplace Transform DBEM for Mixed-Mode Dynamic Crack Analysis", *Computers & Structures*, Vol. 59, 1996, pp. 1021-1031.

[19] Murti, V. and Valliappan, S., "The Use of Quarter Point Element in Dynamic Crack Analysis", *Eng. Fract. Mech.*, Vol. 23, 1986, pp. 585-614.